Reaction Chemistry & Engineering

ROYAL SOCIETY OF CHEMISTRY

PAPER

View Article Online
View Journal | View Issue

Cite this: *React. Chem. Eng.*, 2021, **6**, 1869

Towards controlled bubble nucleation in microreactors for enhanced mass transport†

Renée M. Ripken, [ab] Jeffery A. Wood, [c] Stefan Schlautmann,[b] Axel Günther, [de] Han J. G. E. Gardeniers [b] and Séverine Le Gac *[a]

Received 4th March 2021,
Accepted 14th July 2021

DOI: 10.1039/d1re00092f

rsc.li/reaction-engineering

The interplay of heat and mass transfer in a gas/liquid/solid or heterogeneous catalytic microreactor, in which bubbles grow on a surface, is highly complex. Specifically, distortion of the fluid due to the protrusion and the location of the bubbles can affect transport phenomena, and, in turn, the chemical conversion. Therefore, understanding nucleation and growth of bubbles within microreactors is desirable to optimize reactor performance. A promising approach to that end, and to ultimately control transport phenomena in multiphase catalytic microreactors, is to direct the nucleation of bubbles. For this purpose, we report here a microfluidic device that contains hydrophobic micropits along the smooth floor of a rectangular cross-section microchannel, which were patterned in a silicon substrate using deep reactive ion etching. The pits are intended to act as nucleation sites. Device performance was evaluated for the two cases of boiling of water and outgassing of dissolved carbon dioxide (CO_2). As intended, bubbles were observed to form at the micropits, but also along the rough microchannel side walls. Confocal microscopy revealed that bubbles had spherical shapes, and formed a contact angle with the microchannel floor of >90°. The experimentally determined bubble geometry was used as the boundary condition for a 3D-numerical model. Numerical simulations indicated that the presence of bubbles had a large impact on the local flow distribution, concentration field and reaction conversion within the microreactor, and therefore on the overall conversion for a chosen model reaction.

1. Introduction

During the past twenty years, micro- and nanofabricated structures have been extensively utilized for a wide range of applications that include the efficient determination of fluid and transport properties,[1–5] conducting homogeneous and heterogeneous chemical reactions,[6–8] as well as boiling enhancement.[9–11] In a number of heterogeneous catalytic reactions, gaseous products that are dissolved in a liquid reaction mixture form bubbles on the catalytic surface. One example is aqueous phase reforming (APR), where oxygenated carbohydrates, such as sugars and polyalcohols, are converted to CO, CO_2 and H_2 at a 1 : 1 C : O ratio.[12–18] The presence of bubbles, also depending on their characteristics (size, shape, contact angle with the nucleating surface and stability) can greatly affect the performance of a microreactor, by blocking the active catalytic surface and/or enhancing mass transfer. For example, Neira D'Angelo *et al.* used inert gas to induce Taylor flow in a microchannel to try to reduce mass transport limitations in APR.[19] A very similar dual scenario exists for gas evolving electrodes, as found in fuel cells[20] or other types of electrochemical reactors[21,22] for, *e.g.*, power and hydrogen production, in which bubbles on (micro)-electrodes play an equally important role on the reactor perfomance.[23] In previous work, we numerically investigated the influence of bubbles on the momentum, heat and mass transfer for APR of a 10 wt% glycerol aqueous solution, assuming a 2D-configuration for a microchannel reactor.[24] In that work, hemispherical or elliptical bubbles with contact angles of up to 90° against the catalytic surface were modeled, resulting in a significant coverage of the catalytic surface. This first study indicated that the conversion and the temperature profile in the microreactor are mainly determined by the fraction of the catalytic surface covered by bubbles, with no effect of the bubble protrusion angle.

[a] *Applied Microfluidics for BioEngineering Research, MESA+ Institute for Nanotechnology, TechMed Centre, University of Twente, P.O Box 217, 7500 AE, Enschede, The Netherlands. E-mail: s.legac@utwente.nl; Tel: +31 53 4892722*
[b] *Mesoscale Chemical Systems, MESA+ Institute for Nanotechnology, University of Twente, P.O Box 217, 7500 AE, Enschede, The Netherlands*
[c] *Soft Matter, Fluidics and Interfaces, MESA+ Institute for Nanotechnology, University of Twente, P.O Box 217, 7500 AE, Enschede, The Netherlands*
[d] *Department of Mechanical and Industrial Engineering, University of Toronto, 5 King's College Road, Toronto, ON M5S 3G8, Canada*
[e] *Institute of Biomedical Engineering, University of Toronto, 164 College Street, Toronto, ON, M5S 3G9, Canada*

† Electronic supplementary information (ESI) available. See DOI: 10.1039/d1re00092f

However, depending on the exact (catalytic) surface properties, bubbles can adopt contact angles in excess of 90° and in turn assume more spherical geometries as the surface free energy is minimized.[25,26] Bubbles with contact angles >90° would result in a lower coverage of the (catalytic) surface. They could more easily be released from the surface by fluid shear forces, promising to both reduce the coverage and enhance the conversion at the catalytic surface. An improved understanding of the contact angle and location of the bubbles, as well as the bubble departure radius and time, is therefore desirable to ultimately control transport phenomena in multiphase systems such as APR reaction mixtures. Bubble contact angles can be altered by electric field gradients, an effect that is utilized in electrowetting-on-dielectrics (EWOD) applications,[27,28] by micro- or nanoscale surface roughness elements,[29–34] by changing the wall interfacial tension,[35] or by combining the two latter approaches.[36] Spatial control of bubble nucleation can be achieved by implementing specific microstructures at defined spots on a catalytic surface or electrodes, those structures being known to favor bubble nucleation through modification of the surface wettability.[37–39] Alternatively, the surface chemistry can be altered locally to also change its wettability, for example *via* fluorocarbon deposition to create hydrophobic islands,[21,40,41] which in turns promotes bubble nucleation on those sites.[37] Finally, the bubble detachment size and time have been manipulated using dielectrophoresis,[42] by adding surfactants or polyethylene glycol (PEG) in the solution[22] to change the surface tension and preventing bubble coalescence, by promoting convection using a horizontal magnetic field,[22] by introducing a specific texture or patterning in the catalytic surface,[20] or by applying an ultrasonic field.[43]

Furthermore, in a microreactor it is particularly important that the bubble departure radius, R_d, remains smaller than the hydraulic diameter of the microchannel, to prevent the bubbles from significantly obstructing flow.[44,45] The departure radius (R_d) of a pinned bubble, where the bubble is not in contact with the other microchannel walls, can be derived from the ratio between buoyancy forces and surface tensional forces and expressed as:[46]

$$R_d = \left(\frac{3R_p\sigma}{2\Delta\rho g}\right)^{1/3} \quad (1)$$

where R_p is the radius of the microstructure on which the bubble is pinned, σ the surface tension, $\Delta\rho$ the density difference between the liquid and the gas phases, and g the gravitational constant. A direct consequence of eqn (1) is that the bubble departure radius as well as the bubble detachment frequency, can be notably controlled by either the microstructure size or the surface wettability.[21] Similarly, the microstructure shape can affect the bubble departure radius.[47,48] For instance Yamamoto *et al.*[49] demonstrated that by using saw-tooth shaped micropits instead of randomly shaped defects bubble departure could be promoted *via* surface tension forces. Much can also be learned from research done on nucleate boiling, where bubble detachment from surfaces is relevant for heat transfer.[10,50,51] The detachment of bubbles under shear flow is governed by the balance between the interfacial adhesion forces and the drag force of the fluid,[52] the former being also impacted by the presence of microstructures. Selective use of these different features gives rise to many different potential strategies for affecting and potentially controlling bubble behavior in microreactors.

Here, we report a microreactor with embedded hydrophobic micrometer-sized pits to eventually control bubble nucleation in gas/liquid/solid reactions, such as those that occur in APR. First, the performance of these micropits was tested using both boiling of water and CO_2 outgassing, and the resulting bubble patterns and pinning on the surface were evaluated. Next, confocal microscopy imaging was utilized to determine the shape of these bubbles. Finally, a 3D numerical model was built in COMSOL Multiphysics 5.6 to qualitatively study the influence of such spherical pinned bubbles on the flow and on the resulting concentration profiles for an arbitrary reaction in a microchannel, with or without a catalytic layer. This work provides insight into the effect of high contact angle bubbles growing on a catalytic layer in a multiphase microreactor and how to use the approach of controlled bubble formation, and eventually detachment, to maximize conversion.

2. Materials and methods

Microfluidic device design

To image bubble nucleation and characterize their geometry, a microfluidic device was designed to be fully transparent (Fig. 1) by sandwiching a silicon layer between two glass substrates. A 525 μm deep and 500 μm wide meandering channel was deep reactive ion etched (DRIE) etched through the intermediate silicon substrate. On the backside of the bottom glass layer (numbered 2 in Fig. 1B.), a 65 nm thick indium tin oxide (ITO) layer along with Pt-contacts were sputtered to create an integrated heater. To direct bubble nucleation at well-defined locations in the microchannel, hydrophobic micropits, acting as gas-entrapping cavities,[38] were included in the same glass layer of the device but on the opposing side (Fig. 1B.); these micropits (2 μm in diameter; 1 : 1 aspect ratio) were dry-etched, and subsequently made hydrophobic through fluorocarbon deposition. Finally, the same glass substrate comprised fluidic access ports.

Microfluidic device fabrication

The microfluidic device was manufactured by standard microfabrication techniques using commercially available silicon (100 mm diameter, <100>, p/boron-doped, 525 μm thick, double-side polished, Okmetic) and glass wafers (MEMPax, 100 mm diameter, 500 μm thick, Schott AG). First, a 500 nm thick SiO_2 layer was thermally grown on a silicon

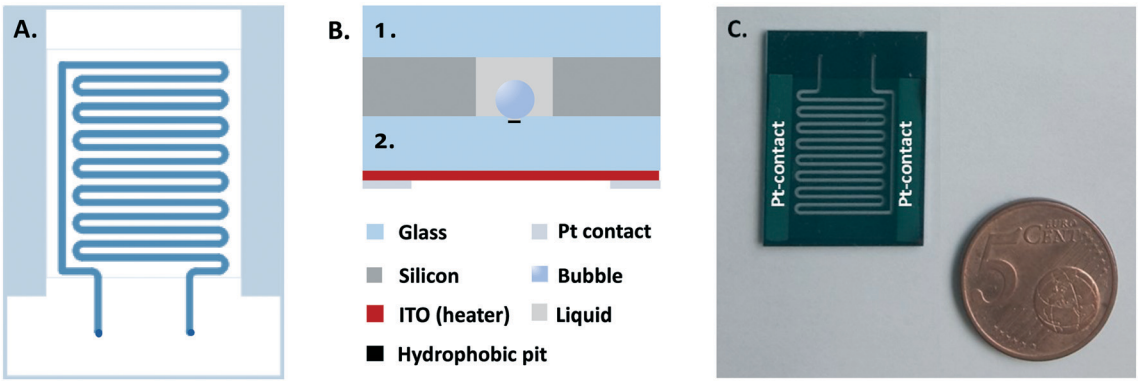

Fig. 1 Microfluidic device for bubble nucleation experiments A. design of the device (top view), with the fluidic channel in blue, the Pt-contacts in light blue-grey, and the inlet and outlet in dark blue; B. schematic representation of the cross-section of the device (not to scale), with the two glass layers numbered 1. and 2., the intermediate silicon layer in gray, the fluidic channel in light gray with a bubble in blue and a hydrophobic micropit in black, C. picture of a device with the Pt-contacts; the actual size of the device is 20.95 mm × 27.95 mm.

wafer (1150 °C), followed by photolithography to transfer the fluidic channel design onto the silicon wafer. The pattern was next etched into the silicon oxide layer by reactive ion etching (Adixen AMS-100). After removing the photoresist, the channels were etched into the silicon by deep reactive ion etching (SPTS Pegasus, Bosch type process with a high etching rate at 0 °C) using the patterned silicon oxide layer as a hard mask. Since the channels were etched though the entire wafer, a second silicon wafer was temporarily attached to the backside of the processed wafer to avoid leakage of the backside cooling gas during etching. Finally, the resulting silicon wafer was cleaned (O_2 plasma, 60 min) and the remaining oxide layer stripped in hydrofluoric acid (50% HF solution) to allow anodic bonding of the silicon surface to glass.

A photolithography step was performed on the bottom glass wafer using a mask containing the micropit pattern, followed by continuous reactive ion etching (Adixen AMS 100, 10 min, 21 sccm C_4F_8, 200 sccm He, 10 sccm Ar, 12 sccm CH_4, ICP 2800 W, CCP 350 W, valve: 15%) to fabricate the micropits. Subsequently, a fluorocarbon film was deposited by plasma-enhanced chemical vapor deposition (PECVD) using an in-house built reactive ion-etching machine (20 °C; 11 W; 25 sccm CHF_3 flow; 130 mTorr; 5 min). Following the deposition, the photoresist and the excess fluorocarbon on top of the photoresist were lifted off in an ultrasonic bath (15 min) in acetone. To produce the fluidic inlet and outlet, the other side of the glass wafer was laminated with Harke i-HE dry film photoresist and exposed to a mask featuring the inlet and outlet design. After development in water, the bottom glass wafer comprising the micropits was protected with an adhesive foil (Nitto SWT 10) and the inlet and outlet were powder-blasted into the glass (in-house built micro-powder blaster; 25 μm diameter Al_2O_3 particles; 5 bar). Afterwards, the foils on both sides were removed.

After cleaning the silicon wafer in piranha solution (H_2SO_4 : H_2O_2, 3 : 1 vol/vol) and the glass wafers successively in acetone and isopropanol, the silicon and processed glass wafers were aligned and anodically bonded (EVG EV-501; 400 °C; 15 min; 1000 V). A second, unprocessed, glass wafer (indicated with 1. in Fig. 1B.) was anodically bonded to the other side of the silicon wafer using the same process parameters as for the first glass wafer to create the 3-layered stack.

The stack was diced into separate devices, which were next individually coated with ITO (in-house built reactive sputter tool) followed by an annealing step to enhance the ITO conductivity (30 min; 400 °C; N_2 atmosphere). Finally, a 100 nm thick platinum layer (in-house sputter tool; 10 min; 200 W) was sputtered on a 10 nm thin tantalum adhesion layer (1 min; 200 W) on the devices using a Kapton foil shadow mask to create the contact pads for the heater.

Microfluidic set-up and experimental procedure

The microfluidic device was placed into a dedicated home-made polyether ether ketone (PEEK) chip holder containing an optical window, allowing microscopic imaging of the fluidic channel (see ESI-1†). A power supply was connected to pushpin connectors incorporated in the top plate of the chip holder, which touched the Pt-contacts on the microfluidic device. A K-type thermocouple was secured onto the glass top layer using yellow Kapton tape to monitor the temperature during the experiments. The fluidic connections consisted of silicone O-rings (ID 1.07 mm and OD 1.27 mm ERIKS) and PEEK ferrules (F-126H, Upchurch). PEEK tubing (ID 0.125 mm and OD 1/32 inch Inacom) was connected to supply fluid flow to the device. A syringe pump (Harvard) and a gastight 250 μL glass syringe (Hamilton) were used to infuse the gas/liquid fluid with a flow rate of 10 μL min^{-1}. In some of the experiments, as specified in the text, no flow was applied.

As the microfluidic device did not contain any catalyst here, bubbles were generated through either boiling of pure MilliQ water or CO_2 outgassing from household sparkling water. In both cases, the device was heated at atmospheric pressure until gas formation was observed.

Confocal microscopy imaging

To evaluate whether concentration gradients can be established at the bubble interface on the catalytic surface, a steady-state regime is desired with static, non-growing or non-departing bubbles. To create such a scenario, the microchannel was perfused with a CO_2/H_2O solution (household sparkling water) at 10 μL min^{-1} and outgassing was induced by shortly heating the device to 45–50 °C, after stopping the liquid flow. By switching off the heater right after the first bubbles were observed, the bubbles could be kept smaller than the channel hydraulic diameter (512 μm). Therefore, the liquid could still freely pass the gas bubbles, preventing local pressure build-up. For confocal microscopy imaging, bubbles were formed through CO_2 outgassing, followed by infusing a 0.001 wt% fluorescein isothiocyanate dextran solution (FITC dextran, average molecular weight 50 kDa, Sigma-Aldrich, Zwijndrecht, The Netherlands) in MilliQ water at a flow rate of 10 μL min^{-1}. Images were recorded using an inverted Nikon A1 confocal microscope.

Numerical model

Geometry & parameters. A 3D-model was developed using a commercial finite element solver (COMSOL Multiphysics 5.6) to study the momentum, the concentration gradient in reagent and the conversion in the microreactor described above, using an arbitrary first-order reaction at steady-state with the aim of demonstrating the possible impact of bubbles on conversion for various cases (moderate and severe mass transport limitations) and the potential benefits of controlled nucleation. A small channel section of 1 cm in length, 500 μm in width and 525 μm in height was considered for numerical simplicity, consisting of 5 × 2 mm repeat units (Fig. 4 shows the repeat unit). Two spherical bubbles with a radius of 180 μm, the distance between the two bubbles centers being 860 μm, were pinned at the silicon side wall in a repeat unit. The location of the catalytic surface, on which the model reaction took place, was varied with respect to the wall on which the bubbles were pinned (see ESI-2† for the configurations of interest).

The microchannel walls were treated as a no-slip interface, and the bubble/liquid interface as no-shear.[53,54] The flow into the domain with the bubbles was assumed as fully developed. The volumetric flow rate was set here at 1 μL min^{-1}, which is 10 times smaller than in the flow experiments; this difference will only scale the results (*via* the residence time). Considering a lower flow-rate in the simulations makes it easier to assess the possible effect of bubbles on the resulting conversion in the microchannel based on the smaller computational domain and see how this is impacted by the degree of mass transport limitations. A substrate with a concentration of 1 mM was introduced at the microchannel inlet, which is sufficiently diluted to apply Fick's law. An arbitrary first-order reaction with an intrinsic surface reaction rate kinetic constant (in m s^{-1}) was considered at the catalytic surface, and a no flux boundary condition was applied to all other interfaces. Several values of intrinsic surface reaction rate constant were simulated, representing moderate and high mass transport limitations. In APR, the extent of reaction or mass-transport limitations depends on the catalyst nature, operating conditions and reacting species.[12,14] The Damköhler numbers of 0.25, 2.5 and 25 were considered, corresponding to moderate, high and higher mass transport limitations. The Damköhler is the ratio between the reaction time scale and the diffusion mass transfer time scale. These Damköhler numbers are found for intrinsic surface reaction rate constants of 5×10^{-7}, 5×10^{-6} and 5×10^{-5} m s^{-1}, which when converted to bulk reaction rates correspond to around 10^{-3}, 10^{-2} and 10^{-1} s^{-1} through multiplying by the ratio of the reaction volume (microchannel minus the inert bubbles) to the catalytic surface area. We considered these values to estimate a plausible effect of bubbles over a range of possible regimes in APR, depending on the nature of the catalyst, specific reaction, *etc.*, and extend into the highly mass transport limiting region in the case of Da = 25. This latter case would be less likely to occur in conventional APR based on reported kinetic constants, although it would potentially be encountered in photoreforming in microreactors.[55,56] A 2nd order Lagrange polynomial basis was used to calculate the concentration profile and the velocity/pressure was calculated using a P2–P1 discretization basis. Mesh independence was assessed through successive refinement of the mesh and examining when the outlet concentration became constant at three decimal places, as well as examining the solution in the case without a catalytic wall which yielded the expected uniform concentration profile at steady-state.

Governing equations. The flow profile in the microchannel was evaluated by solving the Navier–Stokes equations for incompressible fluids:

$$\rho(\vec{u}\cdot\nabla)\vec{u} = -\nabla P + \nabla\cdot\mu[(\nabla\vec{u}) + (\nabla\vec{u})^T] \quad (2)$$

$$\nabla\cdot\vec{u} = 0 \quad (3)$$

with ρ being the density and μ the viscosity of the liquid phase, u the average mean velocity, P the pressure. The bubble walls were treated as slip conditions, with the other microchannel walls treated as no-slip. The density of the fluid was 834 kg m^{-3} and the viscosity 1.2×10^{-4} cP, taken as the values for water at ~500 K and 30 bar, which are representative conditions for APR.[12,14,15,55–58]

The bulk concentration in the microchannel was studied by solving the convection–diffusion equation:

$$\nabla\cdot(-D_c\nabla c + \vec{u}c) = 0 \quad (4)$$

with D_c, the diffusivity constant, taken equal to 1×10^{-9} m^2 s^{-1}, which is the order of magnitude of small substrates at ~500 K and ~30 bar,[12] which are representative conditions for APR.

3. Results and discussion

Device characterization: heater performance and micropit activity

The respective performance of the integrated ITO-based heater and micropits was first evaluated separately. Specifically, a single glass substrate containing a series of micropits placed only along a meandering line (in absence of microchannel) was placed in a tank filled with a supersaturated CO_2 solution, outgassing being induced by reducing the pressure in the tank, to promote bubble nucleation. Microbubbles were observed to form, following the meandering structure with a regular spacing, which is in good agreement with the micropit design (see ESI-3†), and confirms that the microcavities acted as preferential nucleation spots for the bubbles. Next, thermal imaging using an IR camera (FLIR ONE Gen 3 Pro – IOS, resolution 0.1 °C) revealed uniform heating of the microfluidic device by the integrated ITO heater (see ESI-3†). After assembly of the 3-layered stack, the microfluidic devices were finally calibrated for current, power and, most importantly, temperature as a function of the applied voltage (see ESI-4†). This characterization revealed that every device must be calibrated individually, prior to starting experiments.

Controlling bubble formation

Initially, vapor bubbles were created in closed microchannels by boiling of pure MilliQ water in devices with and without micropits. In the reference design (no micropit) explosive boiling was observed at 115 °C, with a sudden apparition of a gas phase in the liquid (Fig. 2A.), which is reminiscent of our previous work.[59] The additional 15 °C above the nominal boiling temperature is indicative of superheating, which is also consistent with the observed boiling mechanism. In contrast, in devices with micropits, the first vapor bubbles already formed at 85 °C (Fig. 2B.), confirming that the presence of hydrophobic microstructures reduced the energy barrier for bubble nucleation, which is consistent with nucleate boiling.

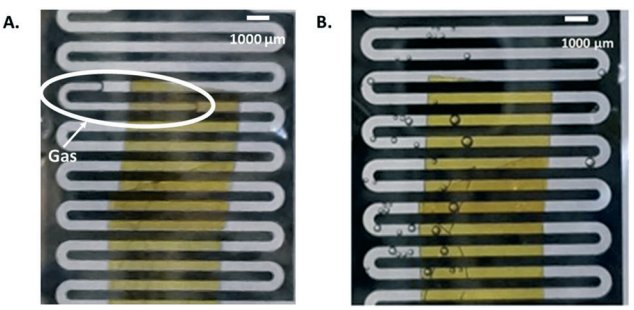

Fig. 2 Vapor bubbles forming in a microchannel without (A.) and with micropits (B.). Without micropits, explosive boiling was observed at 115 °C, with the formation of a large gas plug in the liquid phase. With micropits, however, nucleate boiling was achieved at 85 °C, with the formation of multiple small bubbles in the liquid phase. Kapton tape, in yellow, was used to hold the thermocouple in place.

However, during boiling, bubbles rapidly formed in the liquid phase and their size was difficult to control. A more gentle approach for bubble formation was therefore explored by slowly increasing the temperature at constant ambient pressure in a supersaturated CO_2/H_2O solution; the CO_2 solubility in water decreases, resulting in outgassing, bubble nucleation and further growth. Using this approach, the first bubbles were observed at a temperature as low as 45 °C, and they continued growing as long as heat was applied to the device.

Bubbles typically formed 550 to 1000 µm away from each other (data not shown), which could be explained by the local pressure increase associated with bubble nucleation: if a bubble would nucleate close to another bubble, it would have to overcome a slightly higher pressure. This hypothesis was further supported by the observation that a bubble in close proximity to another already growing bubble, nucleated at a later time than the first bubble.

Bubble stability and micropit deactivation

The microbubble pinning strength in the microchannel was qualitatively characterized by gradually increasing the liquid flow rate. Surprisingly, bubbles remained pinned at their nucleation location in the microchannel for a flow rate of up to 250 µL min^{-1}, indicating strong pinning. The bubbles could still be removed, however, by large gas slugs (see ESI-5†), which formed when a bubble was growing to a size larger than the microchannel hydraulic diameter (bubble length larger than 512 µm).

Repeating the nucleation experiments revealed that micropits deactivated typically after *ca.* 20 cycles of nucleation (see ESI-6†). While the exact deactivation mechanism is unclear, two different phenomena could contribute to it. On one hand, water could fill in the micropits either due to a too high hydrodynamic pressure, or through formation of small microjets after a bubble has collapsed.[60] On the other hand, the force associated with the microjet could damage either the fluorocarbon hydrophobic layer to make the micropits hydrophilic or even the micropit structures, which could be investigated by SEM. Still, it was possible to reactivate the micropits for a further *ca.* 10 cycles

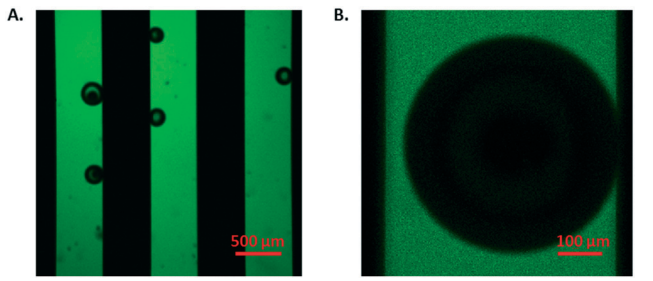

Fig. 3 Confocal microscopy images of the microfluidic channel showing multiple bubbles (A.) or a single bubble (B.) when infusing FITC dextran at a flow rate of 10 µL min^{-1} (bottom view).

of nucleation, by removing the liquid from the entire microfluidic device, followed by heating at 175 °C for 45 min, which suggests that the first envisioned mechanism is most likely at play in the deactivation process. Therefore, no further examination of the pits was conducted to evaluate possible damages.

Bubble shape

To evaluate the 3D bubble geometry and specific location in the channel, confocal microscopy imaging was performed. Fig. 3A. presents three sections of the meandering microfluidic channel with several bubbles. Here, bubbles seemed to systematically nucleate at the side of the channel and not on the hydrophobic micropits at the bottom of the channel, as expected. DRIE-etching of silicon gives rise to defects on the silicon walls, or so-called scallops, which can also be hydrophobic due to the presence of fluorocarbon residues from the dry-etching.[59] Examination of both the micropits and the silicon microchannel wall using high-resolution SEM demonstrated that the micropits were very similar in size as the etching defects, around 2 μm (see ESI-7†), so that both structures could equally act as bubble nucleation sites by lowering the thermodynamic barrier for nucleation.

Next, individual bubbles were further studied to evaluate their morphology and the possible formation of concentration gradients at the bubble interface and/or near the pinning area, using here a fluorescent substance (FITC-dextran). This study first revealed that bubbles were spherical, which is consistent with the presence of a hydrophobic surface and reminiscent of previous work.[36] However, no FITC-dextran concentration gradient could be observed in this microchannel, in which no (catalytic) reaction was performed.

Numerical investigation of the momentum and transport

To investigate the influence of bubbles on the corresponding momentum and mass transport and subsequent reactor performance, a 3D-model was developed in COMSOL Multiphysics 5.6, as detailed in the experimental section.

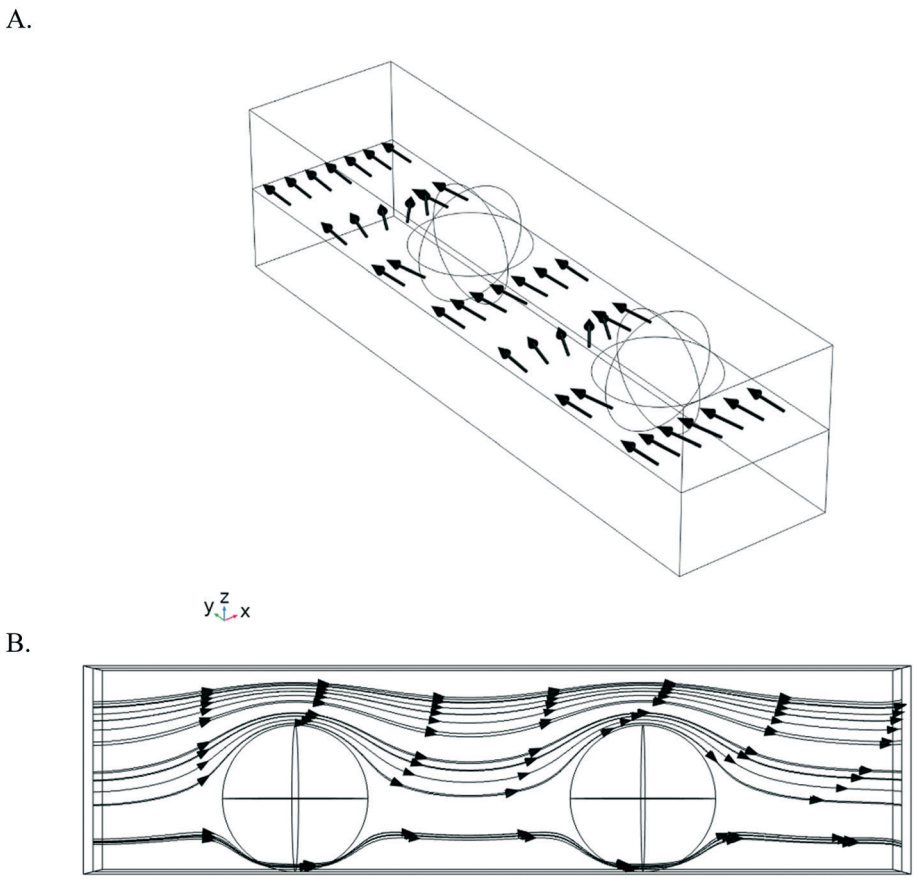

Fig. 4 A. 3D perspective view of a microchannel with bubbles. Default configuration is for bubbles on the side-wall (here: on the right wall). Image can be rotated by 90 degrees for the case where bubbles are on the bottom of the microchannel. Arrows indicate the direction of the flow. For simulations, the cases where the catalyst is on the same wall as the bubbles, on the adjacent wall and on the opposite wall were considered. B. Flow patterns in presence of bubbles. Fluid streamlines for the case with bubbles. Figure represents the top-down view (*xy*-plane) for bubbles on the side wall or the side-view for bubbles the bottom of the microchannel (90 degree rotation between the cases). The case without bubbles represents normal Hagen–Poiseuille flow in a rectangular microchannel (not depicted here).

Table 1 Substrate conversion in a model catalytic reaction for four different configurations of the catalytic layer with respect to the wall on which any bubbles were pinned, as illustrated in Fig. 4, and for various Damköhler numbers corresponding to moderate to serious mass transport limitation scenarios. The conversion was calculated as defined in the text (eqn (5))

	Damköhler number		
Geometry	0.25	2.5	25
No bubbles	0.14	0.57	0.79
Catalyst on the same wall as the bubbles	0.14	0.54	0.73
Catalyst on the adjacent wall with respect to the bubbles	0.14	0.56	0.77
Catalyst on the opposite wall from the bubbles	0.14	0.60	0.85

Negligible concentration differences were found along the microchannel when simulating the case without catalyst, indicating that mesh independence was achieved, as the steady-state solution without a reaction wall should be a uniform concentration. Confocal microscopy imaging, which was done under transient conditions, also showed no observable zones without fluorescence (no gradients were detected) for the time-scale of the experiments (Fig. 3B).

Influence of pinning location of spherical bubbles on the catalytic surface

As a next step, a planar dense catalytic layer with uniform catalytic activity was used in the numerical model to evaluate the effect of bubbles on the conversion for the considered first-order model reaction, for cases ranging from moderate to severe mas transport limitations (Da = 0.25 to 25). Specifically, the conversion was evaluated in four configurations; (i) with no bubbles, and (ii–iv) with both bubbles and a catalytic layer with three different geometries, (ii) both on the same wall, (iii) on opposites walls, or (iv) on adjacent walls. The influence of the configurations on the resulting flow patterns is illustrated in Fig. 4. In all configurations, the reactant conversion was determined (due to the constant flow-rate in and out of the domain) as:

$$X = 1 - \frac{\overline{c}_{\text{out}}}{c_0} \tag{5}$$

where c_0 is the inlet concentration (set arbitrarily at 1 mol m^{-3}) and $\overline{c}_{\text{out}}$ is the average concentration of reactant at the outlet.

As summarized in Table 1, both the presence of bubbles and the respective location of the catalytic layer and the bubbles did impact the conversion rate and, as expected, the extent of this impact depended greatly on the ratio of the reaction to mass transport rate (Da number). For moderate Damköhler numbers (Da = 0.25), all bubble configurations gave approximately the same conversion. As the degree of mass transport limitations increased, differences between these configurations in terms of conversion became apparent. The configuration without bubbles outperformed the one with the bubbles on the same or adjacent wall of the microchannel, while the configuration with the catalyst located on the wall opposite to the bubbles showed the highest conversion. The same trend was also observed at Da = 25, where the magnitude of differences was more pronounced. The difference in conversion between the four configurations can be explained by the impact that the bubbles have on the resulting local flow profiles, as illustrated in Fig. 4. In all configurations with bubbles, the flow squeezes around the bubbles locally, increasing velocity. When the catalyst is on the wall opposite to the bubbles, this periodically results, locally, in a shorter distance over which molecules have to diffuse to reach the catalytic wall. In the configuration where the catalyst is on the same wall as the bubbles, the bubbles act more as an obstacle so that the conversion is minimum out of all simulated configurations. For the configuration where the catalyst is on a wall adjacent to the bubbles, the conversion is slightly reduced compared to the configuration without bubbles for the cases studied here with larger mass transport limitations (Da = 2.5 and 25). For the configuration with the catalyst on the opposite wall, a higher conversion of ~85% was found which represents a relative increase of 8% compared to the configuration with no bubbles for the very high Damköhler numbers (Da = 25). These results, which are reminiscent of previous work leveraging herringbone structures[61] in a microreactor to promote mass transfer towards a catalytic surface,[62] collectively highlight the utility in controlled nucleation in microreactors, as the geometric location of the bubbles was found to have a substantial impact on the overall conversion for all cases simulated with higher Da numbers, and the higher the degree of transport limitations (higher Da), the greater the impact of the bubbles. When considering the potential impact of bubbles on the temperature profiles or available catalytic area, it is clear that the ability to control nucleation of bubbles can have a large positive effect on the overall conversion and performance of a microreactor operating at or in the mass transport-limited regime.

4. Conclusion

Gas bubbles in multiphase microreactors can become a concern if they grow on catalytic surfaces, because they may impede the progress of the reaction by blocking part of the active area. Furthermore, they have an effect on mass transport phenomena, because they change the velocity distribution in the liquid phase that runs through the microreactor channels. In this paper we have approached this rather complex problem by designing and constructing a microfluidic device which has hydrophobic micropits embedded on one of its walls. We have confirmed that with

these pits, which act as preferential nucleation sites, bubble nucleation, growth and departure can be controlled. With a 3D computational fluid dynamics study we have furthermore demonstrated that the exact location of the catalytic layer, with respect to the walls on which bubbles become pinned, matters for substrate conversion: when the bubbles attach on the same wall as the catalyst, conversion drops, whereas the highest conversion occurs when the bubbles and catalyst are on opposite walls. These effects depend on in which direction the velocity distribution in the channel (and therewith mass transport towards the catalytic surface) is forced by the flow obstruction caused by the pinned bubbles.

The observed conversion changes are relatively small but significant, and may become more pronounced by an optimized design in which the catalyst area is patterned along with the position of the nucleation pits. In the current study the gas was considered to be inert. An important element to be included in future studies is the composition of the gas bubbles, *e.g.*, by considering a gas that is involved in the catalytic reaction, such as a gaseous product, since the exact nature of the gas impacts its solubility.[37] In that case, it will be important to remove the gas bubbles from the reactor walls regularly by promoting their detachment. In our experimental work it was observed that the gas bubbles stay pinned up to relatively large flow rates. This may bring the need to actively remove the bubbles with other means, *e.g.*, by inducing vibrations or pressure pulses (*via* integrated) piezoelectric transducers[63] or applying a horizontal magnetic field.[22] Furthermore, for cyclic removal of the pinned bubbles, a different type of micropits than considered in our work has to be developed; our pits have been shown to act as nucleation sites for up to 20 cycles, before becoming inactive. A route to avoid inactivation would be to ensure that not all the gas in the pinned bubble is removed, but to keep some gas trapped to act as a new nucleation point. To that end, highly stable superhydrophobic areas[64] could be created on the microreactor walls.

Conflicts of interest

There are no conflicts to declare.

Acknowledgements

The authors thank Dr. Alváro Moreno Soto for his helpful discussions about bubble nucleation on the single glass substrate. This work was supported by the Netherlands Center for Multiscale Catalytic Energy Conversion (MCEC), an NWO Gravitation programme funded by the Ministry of Education, Culture and Science of the government of The Netherlands and the Natural Sciences and Engineering Council of Canada (RGPIN-2017-06781, AG). Confocal microscopy was in part performed at the Centre for Microfluidic Systems in Chemistry and Biology, supported by the Canada Foundation for Innovation and the Ontario Research Fund.

References

1 M. Abolhasani, E. Kumacheva and A. Gunther, *Ind. Eng. Chem. Res.*, 2015, **54**, 9046–9051.
2 M. Abolhasani, M. Singh, E. Kumacheva and A. Gunther, *Lab Chip*, 2012, **12**, 1611–1618.
3 B. Bao, J. Riordon, F. Mostowfi and D. Sinton, *Lab Chip*, 2017, **17**, 2740–2759.
4 A. Sell, H. Fadaei, M. Kim and D. Sinton, *Environ. Sci. Technol.*, 2013, **47**, 71–78.
5 A. Sharbatian, A. Abedini, Z. B. Qi and D. Sinton, *Anal. Chem.*, 2018, **90**, 2461–2467.
6 N. de Mas, A. Gunther, M. A. Schmidt and K. F. Jensen, *Ind. Eng. Chem. Res.*, 2003, **42**, 698–710.
7 A. Gunther and K. F. Jensen, *Lab Chip*, 2006, **6**, 1487–1503.
8 V. Hessel, P. Angeli, A. Gavriilidis and H. Lowe, *Ind. Eng. Chem. Res.*, 2005, **44**, 9750–9769.
9 H. J. Cho, D. J. Preston, Y. Y. Zhu and E. N. Wang, *Nat. Rev. Mater.*, 2017, **2**, 16092.
10 K. H. Chu, R. Enright and E. N. Wang, *Appl. Phys. Lett.*, 2012, **100**, 241603.
11 L. A. Zhang, E. N. Wang, K. E. Goodson and T. W. Kenny, *Int. J. Heat Mass Transfer*, 2005, **48**, 1572–1582.
12 A. Kirilin, J. Warna, A. Tokarev and D. Y. Murzin, *Ind. Eng. Chem. Res.*, 2014, **53**, 4580–4588.
13 D. Y. Murzin, S. Garcia, V. Russo, T. Kilpio, L. I. Godina, A. V. Tokarev, A. V. Kirilin, I. L. Simakova, S. Poulston, D. A. Sladkovskiy and J. Warna, *Ind. Eng. Chem. Res.*, 2017, **56**, 13241–13254.
14 J. W. Shabaker, R. R. Davda, G. W. Huber, R. D. Cortright and J. A. Dumesic, *J. Catal.*, 2003, **215**, 344–352.
15 J. W. Shabaker and J. A. Dumesic, *Ind. Eng. Chem. Res.*, 2004, **43**, 3105–3112.
16 R. D. Cortright, R. R. Davda and J. A. Dumesic, *Nature*, 2002, **418**, 964–967.
17 J. N. Chheda, G. W. Huber and J. A. Dumesic, *Angew. Chem., Int. Ed.*, 2007, **46**, 7164–7183.
18 R. R. Davda, J. W. Shabaker, G. W. Huber, R. D. Cortright and J. A. Dumesic, *Appl. Catal., B*, 2005, **56**, 171–186.
19 M. F. N. D'Angelo, J. C. Schouten, J. van der Schaaf and T. A. Nijhuis, *Ind. Eng. Chem. Res.*, 2014, **53**, 13892–13902.
20 S. L. Chen, C. T. Lin, C. Pan, C. C. Chieng and F. G. Tseng, *Microfluid. Nanofluid.*, 2009, **7**, 807–818.
21 T. Kadyk, D. Bruce and M. Eikerling, *Sci. Rep.*, 2016, **6**, 38780.
22 D. Fernandez, P. Maurer, M. Martine, J. M. D. Coey and M. E. Mobius, *Langmuir*, 2014, **30**, 13065–13074.
23 A. Angulo, P. van der Linde, H. Gardeniers, M. Modestino and D. F. Rivas, *Joule*, 2020, **4**, 555–579.
24 R. M. Ripken, J. A. Wood, J. G. E. Gardeniers and S. Le Gac, *Chem. Eng. Technol.*, 2019, **42**, 2179–2186.
25 M. Prakash and N. Gershenfeld, *Science*, 2007, **315**, 832–835.
26 D. D. Meng, J. Kim and C.-J. Kim, *J. Micromech. Microeng.*, 2006, **16**, 419–424.
27 S. K. Chung, Y. Zhao and S. K. Cho, *J. Micromech. Microeng.*, 2008, **18**, 095009.

28 J. Li, Y. X. Wang, H. S. Chen and J. D. Wan, *Lab Chip*, 2014, **14**, 4334–4337.
29 E. Gogolides, K. Ellinas and A. Tserepi, *Microelectron. Eng.*, 2015, **132**, 135–155.
30 J. Yong, S. C. Singh, Z. Zhan, F. Chen and C. Guo, *Langmuir*, 2019, **35**, 921–927.
31 W.-B. Jung, G.-T. Yun, Y. Kim, M. Kim and H.-T. Jung, *ACS Appl. Mater. Interfaces*, 2019, **11**, 7546–7552.
32 J. J. Xu, B. D. Chen and T. Z. Z. Xie, *Prog. Nucl. Energy*, 2014, **77**, 1–10.
33 W. Lee, G. Son and J. J. Jeong, *Numer. Heat Transfer, Part B*, 2010, **58**, 323–342.
34 K. H. Chu, R. Xiao and E. N. Wang, *Nat. Mater.*, 2010, **9**, 413–417.
35 J. S. Qin, D. J. Zhou, B. R. Shi, F. H. Chen, L. Luo, A. Kumar, C. Wang, X. Lin, S. Y. Sheng, W. W. Xu, Z. C. Shang, C. T. Cheng, Y. Kuang, W. F. Lin, H. J. Xu and X. M. Sun, *Langmuir*, 2020, **36**, 11422–11428.
36 J. W. Lee, S. Kim, S. Lee and W. Hwang, *Appl. Surf. Sci.*, 2020, **512**, 145709.
37 S. D. Lubetkin, *Langmuir*, 2003, **19**, 2575–2587.
38 M. Blander, *Adv. Colloid Interface Sci.*, 1979, **10**, 1–32.
39 A. Volanschi, W. Olthuis and P. Bergveld, *Sens. Actuators, A*, 1996, **52**, 18–22.
40 P. van der Linde, P. Penas-Lopez, A. M. Soto, D. van der Meer, D. Lohse, H. Gardeniers and D. F. Rivas, *Energy Environ. Sci.*, 2018, **11**, 3452–3462.
41 C. Brussieux, P. Viers, H. Roustan and M. Rakib, *Electrochim. Acta*, 2011, **56**, 7194–7201.
42 C. V. Brown, A. M. J. Edwards, A. Roberts, M. I. Newton, I. C. Sage, R. Ledesma-Aguilar and G. McHale, *Adv. Mater. Interfaces*, 2021, **8**, 2001204.
43 S. D. Li, C. C. Wang and C. Y. Chen, *Electrochim. Acta*, 2009, **54**, 3877–3883.
44 M. J. Jensen, G. Goranovic and H. Bruus, *J. Micromech. Microeng.*, 2004, **14**, 876–883.
45 M. Mohammadi and K. V. Sharp, *J. Fluids Eng.*, 2015, **137**, 0312081–0312087.
46 H. N. Oguz and A. Prosperetti, *J. Fluid Mech.*, 1993, **257**, 111–145.
47 C. A. Stan, A. K. Ellerbee, L. Guglielmini, H. A. Stone and G. M. Whitesides, *Lab Chip*, 2013, **13**, 365–376.
48 M. J. Fuerstman, A. Lai, M. E. Thurlow, S. S. Shevkoplyas, H. A. Stone and G. M. Whitesides, *Lab Chip*, 2007, **7**, 1479–1489.
49 K. Yamamoto and S. Ogata, *Colloids Surf., A*, 2014, **460**, 377–385.
50 Y. Y. Zhu, D. S. Antao, K. H. Chu, S. Y. Chen, T. J. Hendricks, T. J. Zhang and E. N. Wang, *J. Heat Transfer*, 2016, **138**, 091501.
51 J. Mitrovic, *Int. J. Therm. Sci.*, 2006, **45**, 1–15.
52 B. Blackmore, D. Q. Li and J. Gao, *J. Colloid Interface Sci.*, 2001, **241**, 514–520.
53 E. Karatay, P. A. Tsai and R. G. H. Lammertink, *Soft Matter*, 2013, **9**, 11098–11106.
54 O. I. Vinogradova and A. L. Dubov, *Mendeleev Commun.*, 2012, **22**, 229–236.
55 N. A. B. Timmerhuis, J. A. Wood and R. G. H. Lammertink, *Chem. Eng. Sci.*, 2021, **245**, 116835.
56 M. R. K. Estahbanati, M. Feilizadeh and M. C. Iliuta, *AIChE J.*, 2019, **65**, e16724.
57 L. I. Godina, A. V. Kirilin, A. V. Tokarev, I. L. Simakova and D. Y. Murzin, *Ind. Eng. Chem. Res.*, 2018, **57**, 2050–2067.
58 E. W. Lemmon, M. O. McLinden and D. G. Friend, in *NIST Chemistry WebBook, NIST Standard Reference Database Number 69*, ed. P. J. Linstrom and W. G. Mllard, National Institute of Standards and Technology, Gaithersburg, Md, USA, 2018, DOI: 10.18434/T4D303, retrieved on July, 3, 2021.
59 R. M. Ripken, S. Schlautmann, R. G. P. Sanders, J. G. E. Gardeniers and S. Le Gac, *Electrophoresis*, 2019, **40**, 563–570.
60 B. M. Borkent, S. Gekle, A. Prosperetti and D. Lohse, *Phys. Fluids*, 2009, **21**, 102003.
61 A. D. Stroock, S. K. W. Dertinger, A. Ajdari, I. Mezic, H. A. Stone and G. M. Whitesides, *Science*, 2002, **295**, 647–651.
62 S. K. Yoon, G. W. Fichtl and P. J. A. Kenis, *Lab Chip*, 2006, **6**, 1516–1524.
63 G. G. Yaralioglu, I. O. Wygant, T. C. Marentis and B. T. Khuri-Yakub, *Anal. Chem.*, 2004, **76**, 3694–3698.
64 M. Lee, C. Yim and S. Jeon, *Appl. Phys. Lett.*, 2015, **106**, 011605.